J. Fluid Mech. (1995), *vol.* 295, *pp.* 43–60

Flow-history effect on higher modes in the spherical Couette system

By KOICHI NAKABAYASHI AND YOICHI TSUCHIDA
Department of Mechanical Engineering, Nagoya Institute of Technology, Nagoya 466, Japan

(Received 15 November 1991 and in revised form 15 April 1995)

Our flow-visualization and spectral studies of spherical Couette flow between two concentric spheres with only the inner sphere rotating for the clearance ratio (or gap ratio) 0.14 where the Taylor instability occurs have been pursued to systematically explore how and why a variety of wavenumbers and rotation frequencies of the non-axisymmetric periodic disturbances occurs at the same supercritical Reynolds number. The observed periodic disturbances constitute six kinds of disturbances: spiral TG (Taylor–Görtler) vortices, twists developing within toroidal TG vortices, both unmodulated and modulated waves travelling on the TG vortices, and both Stuart vortices and shear waves developing within the Ekman-type secondary flow. Development of these disturbances depends strongly on the flow mode at the initial Reynolds number (initial flow mode) and on the Reynolds-number evolution process approaching the final Reynolds number (acceleration rate and history of the Reynolds number). In our previous studies (Nakabayashi 1983; Nakabayashi & Tsuchida 1988*a*, *b*), we clarified the structures, wavenumbers and rotation frequencies of the periodic disturbances caused by a quasi-static increasing of the Reynolds number. In the present study, we consider how the characteristics of periodic disturbances depend on the following three factors: (i) the rate of increase of the Reynolds number; (ii) the number of toroidal vortices in an initial flow mode; and (iii) the quasi-static Reynolds-number history. The flow modes observed in the present study are all stable to small perturbations, and the transitions among the flow modes are reproducible.

1. Introduction

Spherical Couette flow between two concentric spheres with only the inner sphere rotating shows a spectral laminar–turbulent transition, like circular Couette flow with only the inner cylinder rotating. The spectral transition of circular and spherical Couette flows has attracted attention, because the transition scenario observed in experiments was in good agreement with the new theory of Newhouse, Ruelle & Takens (1978). In both Couette flows, development of the periodic disturbances observed in higher flow modes depends strongly on the flow mode at the initial Reynolds number and on the Reynolds-number evolution process approaching the final Reynolds number. Therefore, a remarkable variety of higher flow modes occurs at the same supercritical Reynolds number through various initial flow modes and Reynolds-number evolutions. Study of the characteristics of higher flow modes provides insight into the physical mechanisms responsible for the spectral transition described above.

Such characteristics were first revealed by Coles (1965) in circular Couette flow. He observed at the same Reynolds number as many as 26 distinct stable flow modes with a different number of Taylor vortices and/or a different wavenumber of azimuthal

waves travelling on the Taylor vortices. The 26 modes in the Taylor and wavy Taylor vortex flows were obtained by approaching the final Reynolds number with different acceleration rates of the inner cylinder rotation and/or by rotating and then stopping the outer cylinder. Following this, Gorman & Swinney (1982) and Rand (1982) showed that the azimuthal waves have a variety of modulation patterns at the same Reynolds number. Subsequently, King *et al.* (1984) and Marcus (1984*a*, *b*) clarified that the wave speed (rotation frequency) detected at the same Reynolds number for the unmodulated or modulated azimuthal waves differs with the number of Taylor vortices or the wavenumber of the azimuthal waves.

Sawatzki & Zierep (1970) were the first to reveal a variety of higher flow modes for spherical Couette flow. They observed up to five distinct stable flow modes showing different friction torques at the same supercritical Reynolds number in the case of small clearance ratios where the Taylor instability occurs. The five flow modes include toroidal or spiral TG vortices (refer to figure 1 for the structure) and/or Stuart vortices developing near the pole in the Ekman-type secondary flow (figures 8 and 9). Subsequently, Wimmer (1976, 1988) showed experimental results indicating that the variety of the above five flow modes is caused by the difference in the acceleration time taken to increase the inner sphere rotation; in other words, by the difference in the rate of increase of the Reynolds number. Wimmer suggested the following explanation for the results: the instability leading to each flow mode requires a particular amount of energy or angular momentum which corresponds to the friction torque measured in each flow mode; consequently the instability depends on the acceleration time during which the required energy or angular momentum is supplied. Wimmer also showed an extensive range of higher flow modes obtained by an increase and/or a decrease of the Reynolds number.

Yavorskaya *et al.* (1980) observed various higher flow modes which include, in addition to the TG vortices described above, travelling waves developing on these vortices and/or a sinusoidal disturbance developing at the equator. The variations were obtained not only by different accelerations of the inner sphere rotation but also by special initial perturbations produced by a temporary rotation of the outer sphere. Subsequently, Bühler & Zierep (1987) investigated experimentally the transition processes from the initial flow modes with different numbers of toroidal vortex cells, and revealed a hysteresis phenomenon in which shear waves developing almost throughout the entire Ekman-type secondary flow (refer to figures 1 and 9) have different wavenumbers and rotation frequencies at the same Reynolds number.

In numerical studies, on the other hand, various axisymmetric higher flow modes with toroidal TG vortices have been simulated by many researchers such as Bonnet & Alziary de Roquefort (1976), Yavorskaya *et al.* (1980), Bartels (1982), Dennis & Quartappelle (1984), Marcus & Tuckerman (1987*a*, *b*), and Bühler (1990). The simulated results concerning friction torques and vortex sizes were in satisfactory agreement with the experimental results described above. However, non-axisymmetric higher flow modes such as periodic, quasi-periodic and aperiodic flow modes have been simulated only recently.

As already mentioned, the higher flow modes in spherical Couette flow include spiral vortices, Stuart vortices and shear waves, in addition to unmodulated and modulated travelling waves (Nakabayashi & Tsuchida 1988*b*) which are similar to those in circular Couette flow. Therefore, various higher flow modes appear more extensively in spherical Couette flow than in circular Couette flow. However, the relations among this extensive variety of spherical Couette flows, with respect to wavenumbers and rotation frequencies of the above periodic disturbances, has not been considered at all.

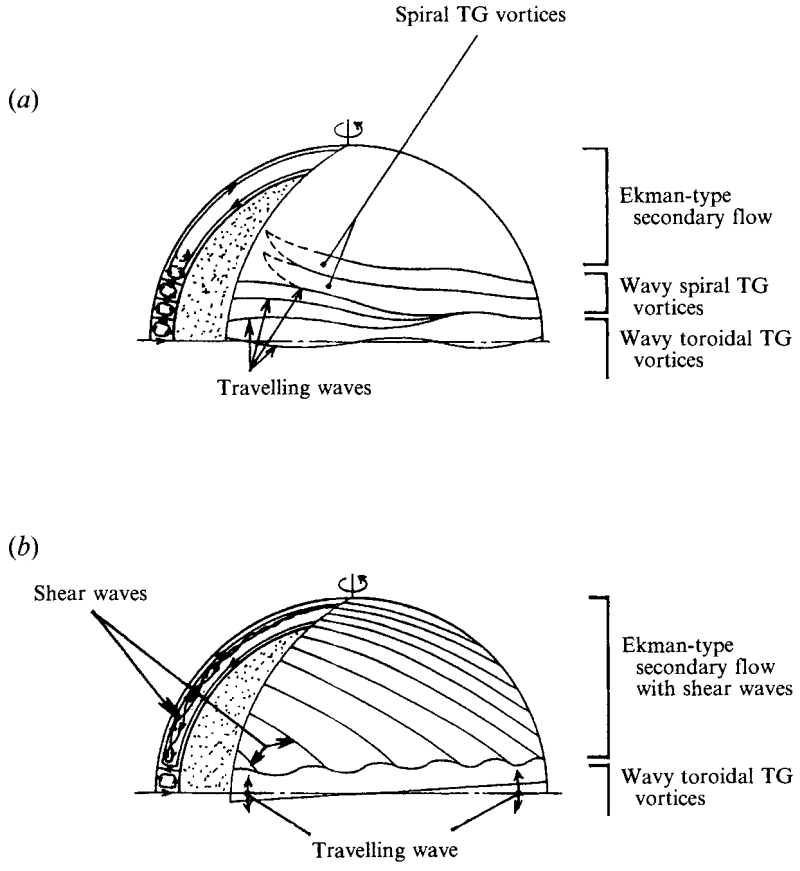

FIGURE 1. Spiral TG vortices, travelling waves and/or shear waves included in (*a*) a wavy toroidal and spiral TG vortex flow (III WTS in table 1) and (*b*) a wavy toroidal TG vortex flow with shear waves (IV WTS_h) in the spherical Couette system with the inner sphere rotating and the outer sphere at rest (Nakabayashi & Tsuchida 1988*a*). These non-axisymmetric disturbances move in the azimuthal direction with each rotation frequency in the laboratory.

The present study was designed to systematically explore how and why such a variety of wavenumbers and rotation frequencies occurs in supercritical spherical Couette flow. We have considered how the characteristics of periodic disturbances in higher flow modes depend on the following three factors: (i) the rate of increase of the Reynolds number; (ii) the number of toroidal vortex cells in an initial flow mode; and (iii) the Reynolds-number history.

The non-axisymmetric higher flow modes such as periodic, quasi-periodic and aperiodic flow modes have only just begun to be simulated, as stated previously. Therefore, our experimental study can serve as a useful guide for forthcoming theoretical and numerical studies. In the future, combined experimental–numerical studies will provide insight into the physical mechanisms responsible for the transitions which occur at higher Reynolds numbers.

2. Experimental techniques

A spherical Couette system with the inner sphere rotating and the outer sphere at rest is characterized by two external control parameters: clearance ratio $\beta = (R_2 - R_1)/R_1$ and Reynolds number $Re = 2\pi \hat{f}_0 R_1^2/\nu$, where R_1 and R_2 are the inner- and

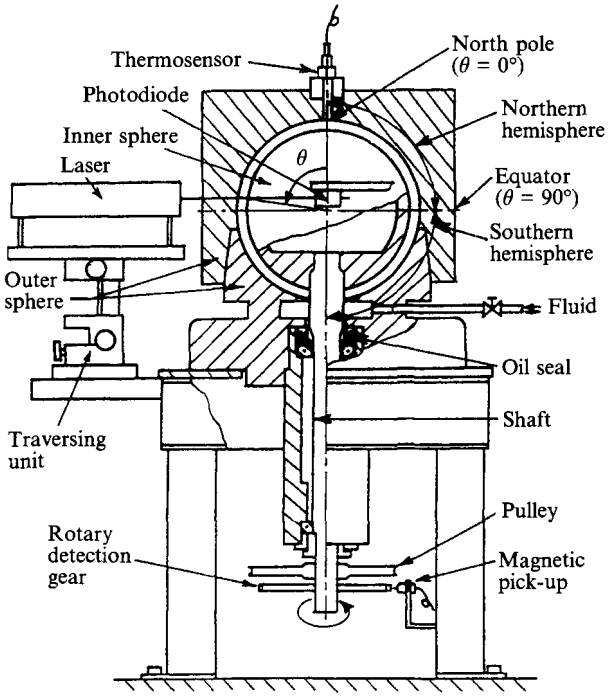

FIGURE 2. Experimental apparatus for the simultaneous spectral and flow-visualization measurements of the intensity of laser light scattered by the aluminium flakes used in flow visualization. θ is the meridian angle (colatitude).

outer-sphere radii, $\hat{f}_0$ is the rotation frequency of the inner sphere, and ν is the kinematic viscosity. Our spherical Couette system (figure 2), presented in detail by Nakabayashi (1983), has $R_1 = 76.89 \pm 0.01$ mm and $R_2 = 87.65 \pm 0.01$ mm, giving $\beta = 0.14$. The initial flow mode and the Reynolds-number evolution process taken to investigate the effects of the three factors described previously are given in each section. The controllable minimum increment or decrement of a reduced Reynolds number R^*, defined as Re/Re_C, was about 0.01 in our spherical Couette system, where the critical Reynolds number Re_C of the Taylor instability was 880. In a quasi-static increase or decrease of R^*, except in the cases of faster changes of the Reynolds number treated in §3, the absolute rate of increase or decrease of R^* was kept at less than 0.0009 s^{-1} so that no shifts were discernible in the transition Reynolds numbers among flow modes.

Wavenumbers and rotation frequencies of periodic disturbances were identified by simultaneous spectral and flow-visualization measurements, as described by Nakabayashi & Tsuchida (1988*a*, *b*). The spectral resolution Δf, defined as $2f_N/N_d$, in the frequency analysis was kept in the range 0.005–0.01 for the Nyquist frequency f_N = 10–20 and the number of time series records of scattered-light intensity detected at a fixed point in the laboratory was $N_d = 2048$ or 4096. Hence, the frequency of each disturbance passing the fixed point, i.e. the fundamental frequency of the velocity fluctuation caused by each disturbance, was resolved to within less than 0.01. Consequently, the rotation frequency of each disturbance, i.e. the fundamental frequency divided by the wavenumber, was resolved to within less than 0.01/wavenumber. In the present study, the frequencies denoted without hats (ˆ) are all scaled by the inner-sphere rotation frequency $\hat{f}_0$ (hatted variables are always dimensional).

3. Influence of the rate of increase of the Reynolds number

We consider the influence of the rate of increase of the Reynolds number on higher flow modes by taking a temporal evolution of the reduced Reynolds number R^* as shown in figure 3. The R^* value is first increased from zero at time $T = 0$ to a specific value $R_S^*(= 2\pi \hat{f}_S R_1^2/(\nu Re_C))$ at $T = T_S$ with a constant rate of increase $\dot{R}^*(= R_S^*/T_S)$, and then kept constant at R_S^* for $T \geqslant T_S$ or $T_h \geqslant 0$. T_S and $T_h(= T - T_S)$ are the time required for the increase and the elapsed time after the increase, respectively. These times are all scaled by a viscous diffusion time $\hat{t}_D$ defined as $(R_2 - R_1)^2/\nu (T = \hat{t}/\hat{t}_D$, $T_S = \hat{t}_S/\hat{t}_D$, etc.). The viscous diffusion time is related to the development of the TG vortices, because that development is due to diffusion of the vorticity produced by the inner-sphere rotation.

In the above Reynolds-number evolution, generally the flow mode or regime changed not only during the increase ($0 \leqslant T < T_S$) but also after it ($T \geqslant T_S$ or $T_h \geqslant 0$), and finally stopped changing. We call the unchanged flow mode observed for $T_h \to \infty$ the final flow mode hereafter. Figure 4 shows a succession of transitions of the flow modes with an increase of T_h at various R_S^* values in the case of $\dot{R}^* = 10^{-0.054}$. For $R_S^* = 2$, for example, the transition from a toroidal vortex flow with four vortices (labelled II T($N = 4$) as described below) to a wavy vortex flow with four vortices and six travelling azimuthal waves (III WT($N = 4$, $m = 6$)) occurs at $T_h \approx 2$, and the transition to a modulated wavy vortex flow mode with four vortices and six modulated travelling waves (III MWT($N = 4$, $m = 6$, $k = 1$)), which becomes the final flow mode, occurs at $T_h \approx 3$.

We now explain the terms 'flow regime' and 'flow mode' used in the present paper. There are four flow regions I–IV in the laminar–turbulent transition of spherical Couette flow: a laminar basic-flow region I, a TG vortex-flow region II, a transition region III and a turbulent flow region IV. The flow regime shows 'flow region' + 'kinds of disturbances', and the flow mode shows 'the flow regime' + 'wavenumbers of the disturbances'. All flow regimes observed in the present study are shown in table 1 with their abbreviations and characteristics. The first abbreviation symbol, e.g. III of III MWT, indicates the above-mentioned flow region. The second symbol, MWT, indicates the kinds of disturbances shown in table 2. Seven kinds of disturbances were observed in the present study. The fundamental frequencies f_M, f_S, ... represent frequencies of the disturbances passing a fixed point in the laboratory. The symbols S_H, S_T, T_W and m represent wavenumbers of the disturbances; $S_P = x - y$ indicates the number of spiral vortex pairs, x pairs in the northern hemisphere and y pairs in the southern hemisphere; N is the number of toroidal vortex cells (i.e. $N/2$ is the number of vortex pairs) in both hemispheres; k is a parameter characterizing a modulation pattern of travelling azimuthal waves as follows. k is related to the phase angle $\Delta\phi$ between the modulation of successive azimuthal waves (m waves) by $\Delta\phi = 2\pi k/m$. Here, $k = -1$ and $m = 6$ shown in figure 4 mean that six successive waves are modulated in sequence in the direction opposite to the wave rotation. Because $\Delta\phi$ is given by $\Delta\phi = -2\pi/6$ and $|\Delta\phi|$ is equal to the azimuthal angle $2\pi/m$ of one wave, waves 1, 6, 5, 4, 3, 2 successively flatten, as shown in figure 14 in Nakabayashi & Tsuchida (1988*b*).

Figure 5 shows how the final flow modes at various R_S^* values depend on the rate of increase $\dot{R}^*$ (the wavenumbers of disturbances are given in the caption). The final flow mode for $1 \leqslant R_S^* < 1.13$, which is a toroidal vortex flow (II T($N = 2$)) developed by the primary instability, is independent of the $\dot{R}^*$ value. However, the final flow modes for $R_S^* \geqslant 1.13$ depend on the $\dot{R}^*$ value, so their variety can be seen. In the range

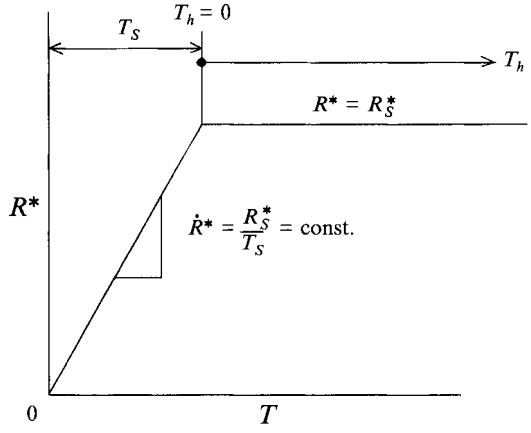

FIGURE 3. The time (T) history of the reduced Reynolds number R^*: R^* is $\dot{R}^*T$ for $0 \leqslant T \leqslant T_S$ and R_S^* for $T \geqslant T_S$, where $\dot{R}^*(= R_S^*/T_S)$ is the rate of increase of the Reynolds number. This was used to investigate a variety of final flow modes which occur for $T_h \to \infty$ at $R^* = R_S^*$ by taking different values of $\dot{R}^*$.

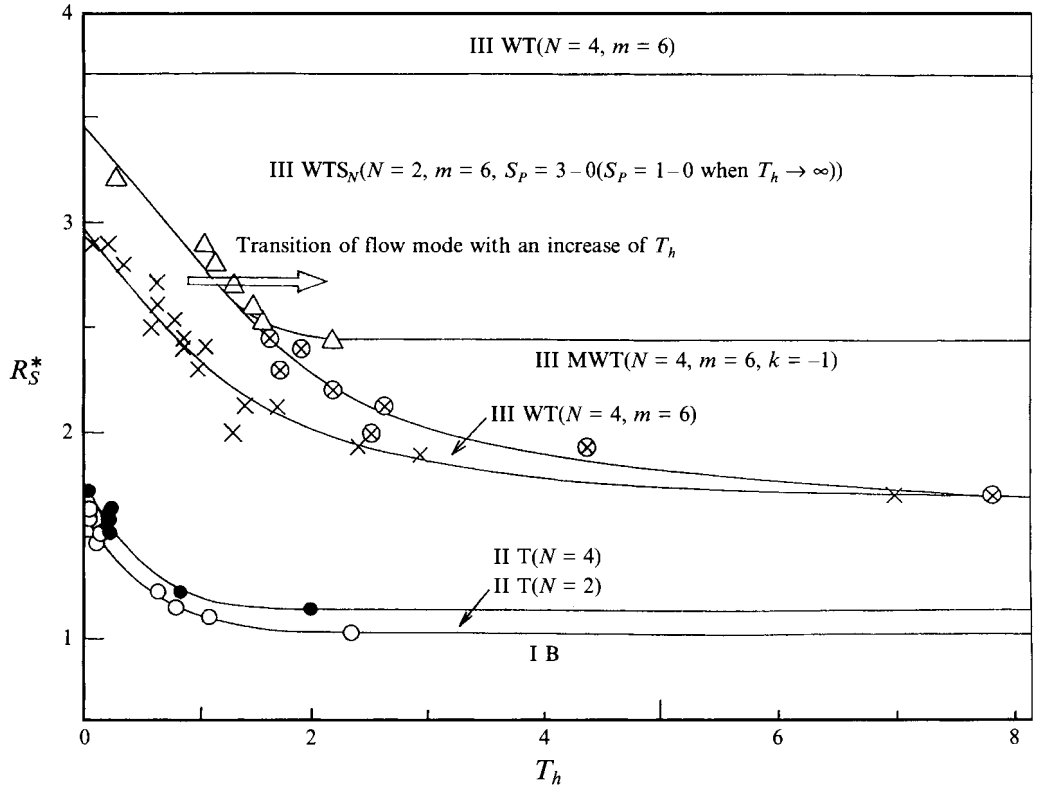

FIGURE 4. A succession of transitions of the flow modes with an increase of T_h at various R_S^* values for $\dot{R}^* = 10^{-0.054}$. Refer to tables 1 and 2 for the flow regimes II T, III WT, III MWT, ... and the wavenumbers N, m, ... of disturbances, respectively.

Flow regime	Characteristics
I B	Laminar flow + secondary flow (laminar basic flow)
II T	Laminar flow + toroidal TG vortex + secondary flow
II TS	Laminar flow + spiral and toroidal TG vortices + secondary flow
III B	Laminar flow + secondary flow (supercritical basic flow)
III MWT	Laminar flow + modulated wavy toroidal TG vortex + secondary flow
III S_h	Laminar flow + secondary flow with shear waves
III T	Laminar flow + toroidal TG vortex with strong circulation + secondary flow
III TS_t	Laminar flow + toroidal TG vortex + secondary flow with a Stuart vortex
III $T_w S_t$	Laminar flow + twisted toroidal TG vortex + secondary flow with Stuart vortices
III WS	Laminar flow + wavy spiral TG vortex + secondary flow
III WT	Laminar flow + wavy toroidal TG vortex + secondary flow
III WTS	Laminar flow + wavy toroidal and spiral TG vortices + secondary flow
IV S_h	Turbulent flow + secondary flow with shear waves
IV WTS_h	Turbulent flow + wavy toroidal TG vortex + secondary flow with shear waves

TABLE 1. Abbreviations for and characteristics of all flow regimes observed

Label	Kind of disturbance	Symbol	Fundamental frequency
M	Modulation of travelling waves	k	f_M
S	Spiral TG vortices (S_N, S_S)	$S_P = x-y$	f_S
S_h	Shear waves	S_H	f_H
S_t	Stuart vortices	S_T	f_U
T	Toroidal TG vortices	N	—
T_w	Twists within toroidal TG vortices	T_W	f_T
W	Travelling waves	m	f_W

TABLE 2. Kinds, wavenumbers and fundamental frequencies of all disturbances. k is a modulation parameter; $S_P = x-y$ indicates the number of spiral TG vortex pairs, x pairs in the northern hemisphere and y pairs in the southern hemisphere; N is the number of toroidal TG vortex cells in both hemispheres. $f_M, f_S, \ldots$ represent the fundamental frequencies of the velocity fluctuation caused by periodic disturbances. S_N and S_S indicate the spiral TG vortices which occur in the northern and southern hemispheres, respectively.

$1.13 \leqslant R_S^* \lesssim 1.7$, we obtained two final flow modes, a singly periodic toroidal and spiral vortex flow (II TS($N = 2$, $S_P = 3-3$)) and a toroidal vortex flow (II T($N = 4$)), because six pairs of spiral vortices or a pair of toroidal vortices develop additionally in the above-described flow mode II T($N = 2$) for a small or large rate of increase. This result shows that the larger rate of increase, i.e. the shorter increase time, still makes the vortex structure stationary.

In the range $1.7 \lesssim R_S^* \lesssim 2.5$, we obtained two doubly periodic flow modes as the final flow mode: a modulated wavy toroidal flow (III MWT($N = 4$, $m = 6$, $k = -1$)) and a wavy toroidal and spiral flow (III WTS($N = 2$, $m = 6$, $S_P = 3-3$)), where the wave modulation occurs only in the absence of spiral TG vortices.

For $R_S^* \gtrsim 2.5$, doubly periodic, singly periodic, intermittent and/or time-independent flow modes occur, depending on the $\dot{R}^*$ value. For larger rates of increase ($\dot{R}^* \gtrsim 10^{-0.5}$), a doubly periodic flow mode, III WTS_N($N = 2$, $m = 6$, $S_P = 1-0$), III WTS_S($N = 2$, $m = 6$, $S_P = 0-1$) or III WS($m \approx 6$, $S_P = 1-1$), occurs. For smaller rates ($\dot{R}^* \lesssim 10^0$), however, a singly periodic flow mode (III WT($N = 4$, $m = 6$)) occurs. Particularly for smaller rates ($\dot{R}^* \lesssim 10^{-0.5}$) in the range $2.64 \lesssim R_S^* \lesssim 2.8$, an intermittent

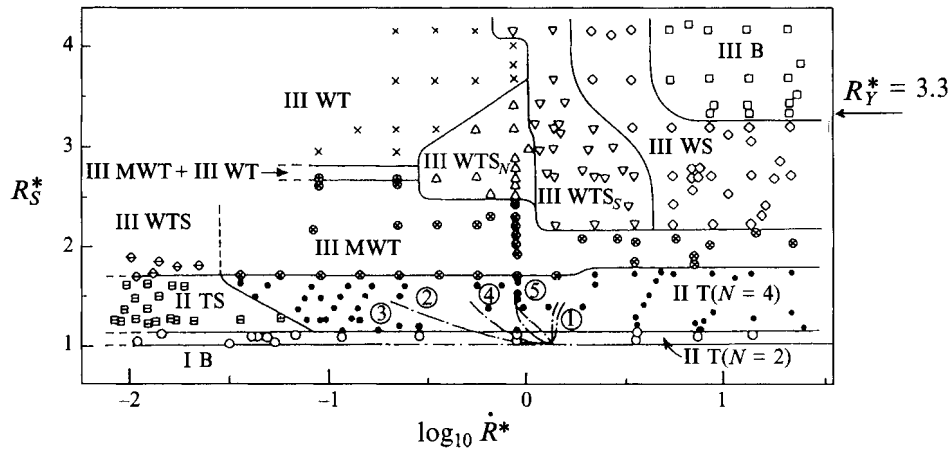

FIGURE 5. Dependence of final flow modes on $\dot{R}^*$ and R_S^*. Present data for $\beta = 0.14$: ○, II T(N = 2); ⊟, II TS($N = 2$, $S_P = 3-3$); ●, II T($N = 4$); ⋄, III WTS($N = 2$, $m = 6$, $S_P = 3-3$); ⊗, III MWT($N = 4$, $m = 6$, $k = -1$); ×, III WT($N = 4$, $m = 6$); ⊕, III MWT($N = 4$, $m = 6$, $k = -1$) + III WT($N = 4$, $m = 6$); △, III WTS$_N$($N = 2$, $m = 6$, $S_P = 1-0$); ▽, III WTS$_S$($N = 2$, $m = 6$, $S_P = 0-1$); ◇, III WS($m \approx 6$, $S_P = 1-1$); □, III B. Wimmer's (1976) data for $\beta = 0.18$: 1, mode I [corresponds to III B]; 2, indistinct mode; 3, mode III [II T($N = 2$)]; 4, mode IV [II T($N = 4$)]; 5, mode V [probably III WS]. R_Y^* is the lower limit of the Reynolds number at which the III B regime was observed for $\beta = 0.14$ by Yavorskaya *et al.* (1980).

flow mode (III MWT($N = 4$, $m = 6$, $k = -1$) + III WT($N = 4$, $m = 6$)) appears, where six travelling waves are modulated and unmodulated at intervals of several minutes. This intermittent wave modulation is the same as that reported in Nakabayashi & Tsuchida (1988*b*). Such a temporally repeating phenomenon also occurs near the boundary ($R_S^* = 1.13$) between II T($N = 2$) and II T($N = 4$), where the toroidal cell immediately next to the Ekman secondary flow in each hemisphere appears and disappears at the same intervals as the above case. These two temporally repeating phenomena do not occur for the case with spiral vortices. This fact shows that such an intermittency occurs only in the marginal states which strongly resist a spiral disturbance. On the other hand, for much larger rates of increase ($\dot{R}^* \gtrsim 10^{0.7}$) for $R_S^* \gtrsim 3.3$, a time-independent supercritical basic flow (III B) occurs which was also reported by Wimmer (1976) and Yavorskaya *et al.* (1980). The lower limit ($R_S^* \approx 3.3$) of its occurrence in the present study agrees with that ($R_Y^* = 3.3$) reported by Yavorskaya *et al.*

The five flow modes obtained for $\beta = 0.18$ by Wimmer (1976) are shown in domains 1–5 in figure 5: mode I (corresponding to the supercritical basic flow III B in the present study) in domain 1; mode II (two-vortex flow II T($N = 2$)) in 3; mode IV (four-vortex flow II T($N = 4$)) in 4; mode V (probably wavy spiral vortex flow III WS) in 5; and the indistinct mode in 2. It is evident from the comparison between the present results and Wimmer's that the rate of increase does not affect the range $1 \leqslant R_S^* < 1.13$ (II T($N = 2$)) for $\beta = 0.14$ but does affect all $R_S^* \geqslant 1$ for $\beta = 0.18$.

Yavorskaya *et al.* (1980) conjectured that the occurrence of the supercritical basic flow (III B) described above was due to the large difference between the spin-up time and the viscous diffusion time. So we investigated the relationship among spin-up time ($\hat{t}_{SP} = (R_2 - R_1)/(2\pi \hat{f}_S \nu)^{0.5}$), viscous diffusion time ($\hat{t}_D = (R_2 - R_1)^2/\nu$), Reynolds-number increase time ($\hat{t}_S = T_S \hat{t}_D$) and the final flow mode at $R_S^*(= 2\pi \hat{f}_S R_1^2/(\nu\, Re_C))$ using the experimental results shown in figure 5. The relationship is summarized in

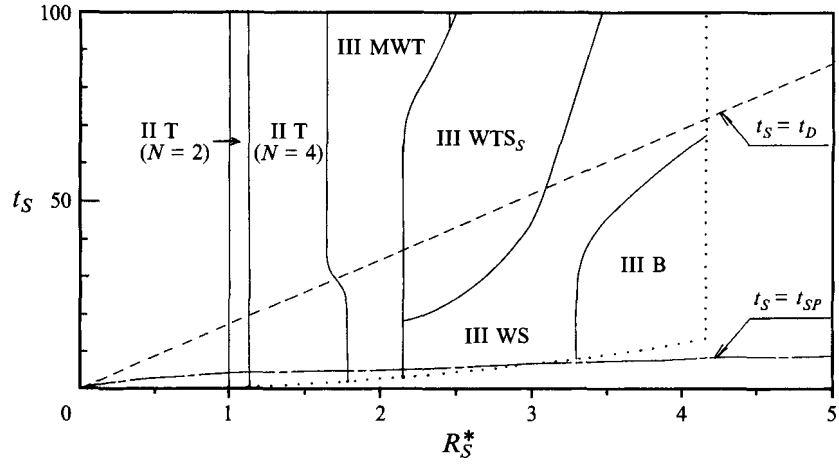

FIGURE 6. The dependence of Reynolds-number and its rate of increase on the final flow modes shown in figure 5. t_S, t_D and t_{SP} are acceleration time, viscous diffusion time and spin-up time, respectively, where $t_D = t_{SP}^2$.

figure 6, where the final flow mode is shown in the R_S^*, t_S parameter plane; t_S $(= \hat{t}_S/\hat{t}_0)$, t_{SP} $(= \hat{t}_{SP}/\hat{t}_0 = \beta\, Re_C^{0.5}\, R_S^{*0.5})$ and t_D $(= \hat{t}_D/\hat{t}_0 = t_{SP}^2)$ are the increase time, spin-up time and diffusion time, respectively, scaled by $\hat{t}_0 = 1/(2\pi\hat{f}_S)$; the boundaries among the final flow modes were obtained from the transformation $t_S = \beta\, Re_C\, R_S^{*2}/\dot{R}^*$; and the limit of the present measurements is shown by the dotted line. The supercritical basic flow III B occurs only under the condition $t_S < t_D$ for $R_S^* \gtrsim 3.3$ where the t_D value is more than 7.5 times the t_{SP} value. This result is explained as follows. The TG vortices appear for the large viscous diffusion time t_D, as described previously, while the Ekman-type secondary flow develops for the shorter spin-up time t_{SP}. Therefore, provided that the difference between the t_{SP} and t_D values is great, the Ekman-type secondary flow has time to redistribute the angular momentum in the spherical gap in such a way as to suppress the TG-type instability, and consequently the supercritical basic flow is observed. The variation of the other flow modes in the parameter plane also depends on the combination of t_{SP} and t_D values.

4. The influence of the number of toroidal TG vortex cells in the initial flow mode

In spherical Couette flow, we can observe two types of disturbances: cylinder and disk types. The cylinder-type disturbances, which are similar to those observed in circular Couette flow, are TG vortices and higher-order disturbances such as travelling waves and wave modulation which occur on/in the vortices. The disk-type disturbances, which are similar to the cross-flow-type disturbances developing in the Ekman boundary layer on a disk rotating in a casing, are both Stuart vortices and shear waves developing within the Ekman-type secondary flow.

For $\beta = 0.14$, we observed flow modes with four, two or zero toroidal vortex cells ($N = 4$, 2 or 0). As described later, the characteristics of the cylinder-type disturbances observed for $N = 4$ and 2 strongly depend on the value of N. This is thought to be closely related to the result that the equator, at which centrifugal forces are greatest, is a vortex outflow boundary for $N = 4$ whereas it is a vortex inflow boundary for

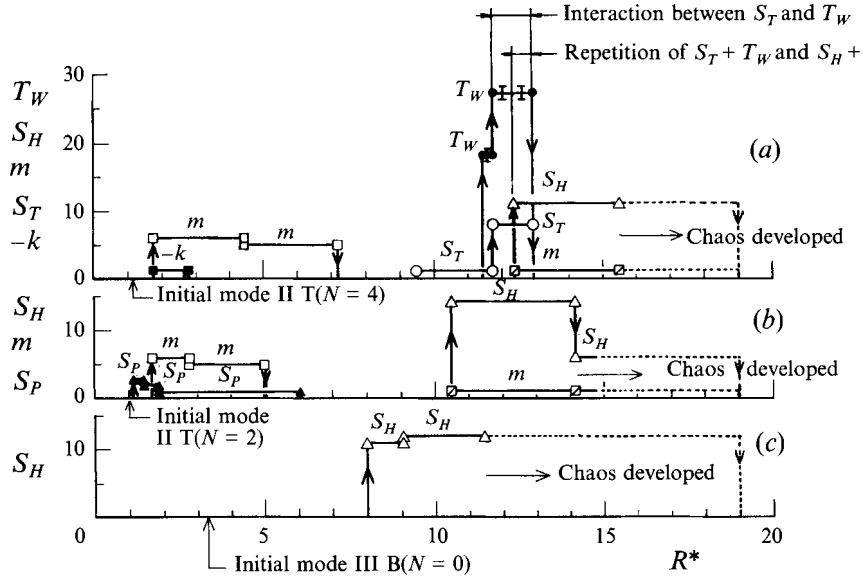

FIGURE 7. Reynolds-number dependence of wavenumbers of the periodic disturbances observed in the quasi-static laminar–turbulent transition from three initial flow modes III B($N = 0$), II T($N = 2$) and II T($N = 4$) to $R^*_{max} = 20$, where each N value remained constant until the R^*_{max} value. Refer to table 2 for the wavenumbers T_W, S_H, m,.... The S_H and m values indicated by broken lines were unmeasurable owing to developing chaos. (*a*) $N = 4$. (*b*) $N = 2$. (*c*) $N = 0$.

$N = 2$. Also, the characteristics of the disk-type disturbances observed for $N = 4$, 2 and 0 depend on N. This is connected with the fact that the extension of the Ekman-type secondary flow changes with N. Hence, the direction of the secondary flow of the vortices and the extension of the Ekman-type secondary flow have a significant influence on the characteristics of disturbances in higher flow modes. To consider this influence, we investigate the N dependence of the characteristics of cylinder- and disk-type disturbances in this section.

We first produced three initial flow modes, II T($N = 4$), II T($N = 2$) and III B($N = 0$), following the experimental procedure described in §3. Then, we investigated the wavenumbers and rotation frequencies of the cylinder- and/or disk-type disturbances observed in the quasi-static laminar–turbulent transitions from the above three initial flow modes. Each N value remained constant until the largest Reynolds number, $R^*_{max} = 20$, reached in the present experiment. The characteristics of the disturbances obtained for $N = 2$ agreed with those reported in Nakabayashi & Tsuchida (1988*a*).

Figure 7(*a–c*) shows the R^* dependence of the wavenumbers of cylinder- and disk-type disturbances in laminar–turbulent transitions for $N = 4$, 2 and 0, respectively. The cylinder-type disturbances, travelling waves (m), wave modulation (k), twists (T_W) and spiral vortices (S_P), are influenced by the different N values as follows. The wavenumber of the travelling waves changes with increasing R^* in the same way for $N = 4$ and 2, i.e. $m = 6 \rightarrow 5 \rightarrow 0 \rightarrow 1$, but the transition Reynolds numbers change distinctly with N. The wave modulation and twists occur for $N = 4$, but not for $N = 2$. The spiral vortices, on the other hand, occur for $N = 2$, but not for $N = 4$. These results show that the number of toroidal vortices has a strong influence on the higher-order disturbances of the vortices, namely the secondary-flow direction and extent of the vortices have an important role in the cylinder-type disturbances. The twists described above appear within all four toroidal cells, and have a periodic rope-like

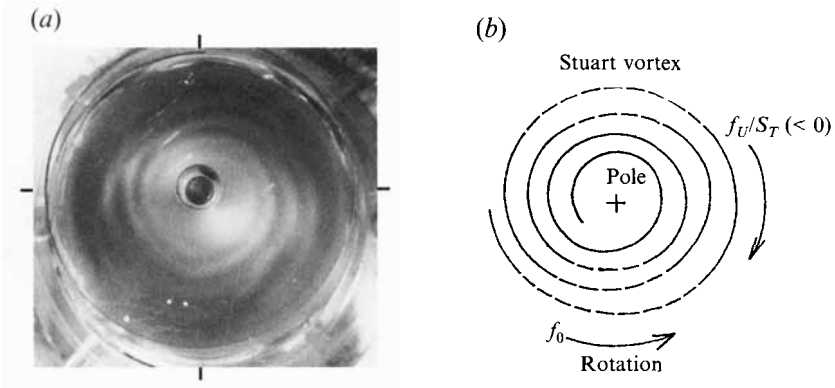

FIGURE 8. TG vortex flow III $TS_t(N = 4, S_T = 1)$ with four toroidal vortices and one Stuart vortex at $R^* = 10.5$. f_U/S_T (negative value) and f_0 are the rotation frequencies of the Stuart vortex and the inner sphere, respectively, in the laboratory. (*a*) Photograph taken in the pole direction. (*b*) Schematic of the photograph (*a*).

structure similar to that in circular Couette flow (Andereck, Dickman & Swinney 1983). The rotation frequency f_T/T_W is almost 0.19 for $T_W \approx 18$, independent of the R^* value.

Disk-type disturbances are also influenced by different N values. Shear waves (S_H) occur for each of $N = 4$, 2 and 0, but the onset Reynolds number and wavenumber differ markedly with N. The onset Reynolds number becomes smaller as the Ekman-type secondary flow extends a greater distance towards the equator. Stuart vortices (S_T) occur for $N = 4$, but not for $N = 2$ and 0. Figure 8 shows the Stuart vortex ($S_T = 1$) observed for $9.5 \leqslant R^* < 11.8$. This Stuart vortex has a clockwise spiral pattern from the pole to the equator, as reported by Sawatzki & Zierep (1970), Wimmer (1976) and Bühler & Zierep (1987), and develops near the pole ($20° \lesssim \theta \lesssim 50°$) in the Ekman-type secondary flow. The Stuart vortex is completely different from the shear wave, which has a counterclockwise pattern and develops within almost the whole Ekman-type secondary flow (refer to figures 1 and 9). The Stuart vortex in figure 8 rotates with a constant frequency in the direction opposite to the inner sphere; the rotation frequency f_U/S_T is almost -1, independent of the R^* value. Wimmer (1976) and Bühler & Zierep (1987) reported that Stuart vortices are stationary, i.e. $f_U/S_T = 0$ for $\beta = 0.18$. Hence, the rotation frequency depends on β.

Interaction between the disk- and cylinder-type disturbances was observed in the range $11.8 \leqslant R^* < 13$ for $N = 4$, as shown in figure 7(*a*). First, at $R^* = 11.8$, the wavenumber variations of Stuart vortices ($S_T = 1 \rightarrow 8$) and twists ($T_W \approx 18 \rightarrow 27$) occur simultaneously, together with their simultaneous rotation-frequency variations ($f_U/S_T = -1 \rightarrow +0.07, f_T/T_W = 0.19 \rightarrow 0.14$). It should be noted here that the Stuart vortices begin to rotate in the same direction as the inner sphere instead of in the opposite direction; and the Stuart vortices can rotate in either direction ($f_U/S_T < 0$ and > 0), depending on the Reynolds number. When R^* reaches 12.4, a travelling wave and eleven shear waves occur with turbulence followed by temporal repetition of two flow modes, III $T_w S_t(m = 0, T_W \approx 27, S_T = 8)$ and IV $WTS_h(m = 1, T_W = 0, S_H = 11)$. In this temporal repetition, the Stuart vortices and twists alternate with the travelling wave and shear waves at intervals of about thirty minutes. This temporal repetition was observed near the pole, as shown in figure 9. Figure 9(*a*) shows Stuart vortices which have a clockwise spiral pattern from the pole to the equator. Figure 9(*c*) shows shear waves with the counterclockwise pattern. The transient crossing of the

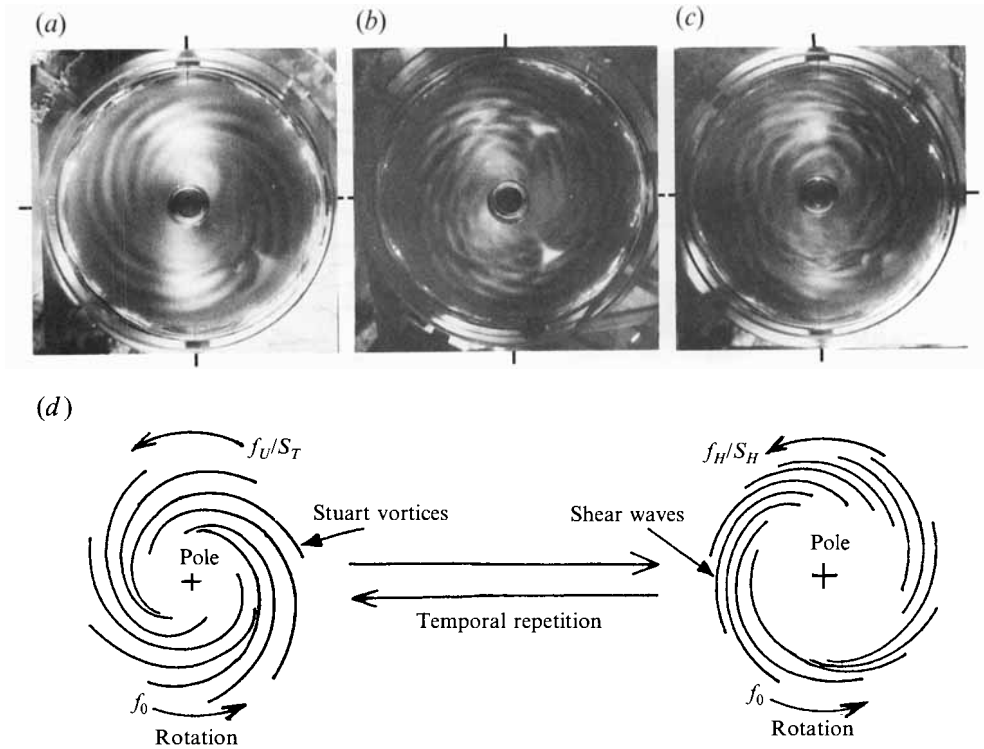

FIGURE 9. Temporal repetition of two flow modes: a non-turbulent twisted TG vortex flow with four toroidal vortices, about twenty-seven twists and eight Stuart vortices (III $T_w S_t$($N = 4$, $T_W \approx 27$, $S_T = 8$)); and a turbulent wavy toroidal TG vortex flow with four toroidal vortices, one azimuthal wave and eleven shear waves (IV WTS_h($N = 4$, $m = 1$, $S_H = 11$)), at $R^* = 12.5$. f_U/S_T, f_H/S_H and f_0 are the rotation frequencies of the Stuart vortices, the shear waves and the inner sphere, respectively, in the laboratory. (*a*) Photograph of III $T_w S_t$($N = 4$, $T_W \approx 27$, $S_T = 8$). (*b*) Photograph of the superposition of III $T_w S_t$ and IV WTS_h. (*c*) Photograph of IV WTS_h($N = 4$, $m = 1$, $S_H = 11$). (*d*) Schematic of the temporal repetition of III $T_w S_t$ (left side) and IV WTS_h (right side).

Stuart vortices and the shear waves is presented in figure 9(*b*). The temporal repetition finishes at $R^* = 13$ with the disappearance of the Stuart vortices and twists.

Next, we consider in figure 10 how the relationship between the rotation frequency f_W/m of travelling waves and the R^* value differs with N. The rotation frequency is independent of N for $R^* \lesssim 2.2$, but it depends on N for $R^* \gtrsim 2.2$ although it has a similar tendency to decrease with an increase of R^* for both $N = 4$ and 2. The rotation-frequency variation with the wavenumber is different between $N = 4$ and 2, i.e. it is stepwise for $N = 4$ but not for $N = 2$. The rotation frequency for $m = 5$ definitely differs between $N = 4$ and 2. A similar result was reported by King *et al.* (1984) in circular Couette flow, in which the rotation frequency of travelling azimuthal waves differs with the number of Taylor vortex cells. In the present study, the f_W/m value for $N = 2$ is smaller than for $N = 4$. This is conjectured to be due to the fact that the travelling waves for $N = 2$ coexist with the spiral vortices, which have a lower rotation frequency (about 0.43) than the travelling waves (Nakabayashi & Tsuchida 1988*a*). Therefore, the travelling waves for $N = 2$ are influenced by the spiral vortices, so that the f_W/m value for $N = 2$ is smaller than for $N = 4$.

The rotation frequencies of disk-type disturbances are also influenced by N. Figure 11 shows that the rotation frequency f_H/S_H of shear waves depends on N as well as on

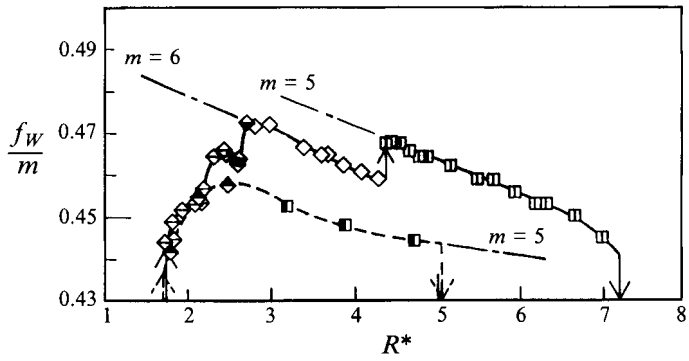

FIGURE 10. Reynolds-number dependence of the rotation frequency of the travelling waves observed for $N = 4$ (——) and $N = 2$ (---). Results for $N = 4$: ⟐, $m = 6$ ($k = -1$) in III MWT; ◫, $m = 5$ in III WT; ⬙, $m = 6$ ($k = -1$) + 6 in III MWT + III WT (the wave modulation with $k = -1$ alternately appearing and disappearing in six travelling azimuthal waves); ◇, $m = 6$ in III WT. Results for $N = 2$: ⟐, $m = 6(S_p = 2-0$ for $1.71 \leqslant R^* < 1.93$ and $S_p = 1-0$ for $1.93 \leqslant R^* < 2.80)$ in III WTS_N; ◧, $m = 5(S_p = 1-0)$ in III WTS_N.

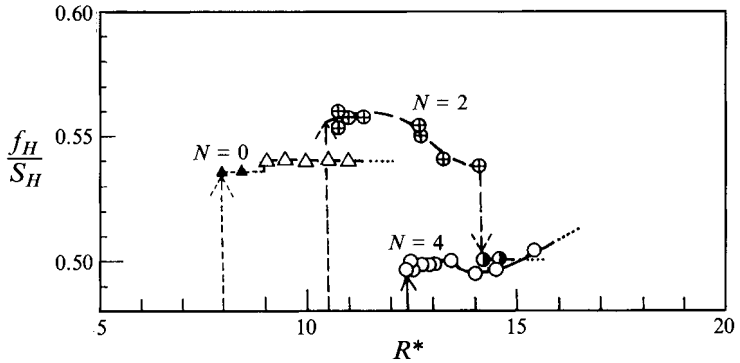

FIGURE 11. Reynolds-number dependence of the rotation frequency of the shear waves observed for $N = 4$ (——), 2 (---) and 0 (-----). Results for $N = 4$: ○, $S_H = 11(m = 1)$ in III $T_w S_t$ + IV $WTS_h(12.4 \leqslant R^* < 13.0)$ and IV $WTS_h(R^* \geqslant 13.0)$. Results for $N = 2$: ⊕, $S_H = 14(m = 1)$ in IV WTS_h; ◑, $S_H \approx 6(m = 1)$ in IV WTS_h. Results for $N = 0$; ▲, $S_H = 11$ in III S_h; △, $S_H = 12$ in IV S_h. The dotted line shows that the rotation frequencies were unmeasurable owing to developing chaos.

the wavenumber S_H. The rotation frequency increases with wavenumber for both $N = 2$ and 0. This occurs when R^* is increased in the case $N = 0$ and when R^* is decreased for $N = 2$.

5. Hysteresis phenomenon

It is widely accepted that hysteresis occurs in closed flows. In this section we consider how hysteresis appears in spherical Couette flow. Figure 12 shows two examples of hysteresis obtained when the Reynolds number R^* is first increased from an initial flow mode and then decreased quasi-statically, in the R^*, N, m parameter space. N is the number of toroidal TG vortex cells and m is the wavenumber of travelling waves. The first example obtained for the initial flow mode with a state of $N/m = 4/0$ at $R^* = 1.13$ (point A on figure 12) is as follows. When R^* is first increased from 1.13 (A) to 4.42 (E), we observe successive state transitions, $4/0 \rightarrow 4/6(k = -1)$ (B) $\rightarrow 4/6$ (D) $\rightarrow 4/5$

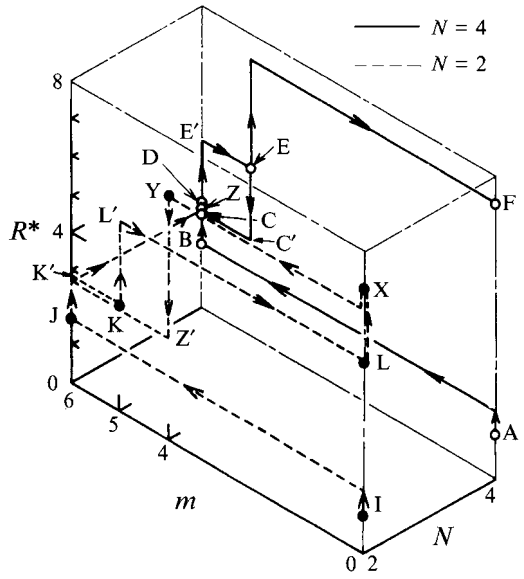

FIGURE 12. Two examples of the hysteresis phenomenon shown in the R^*, N, m parameter space. The N/m state, flow regime and R^* value at each point are as follows: A, 4/0 in II T at $R^* = 1.13$; B, $4/6(k=-1)$ in III MWT at $R^* = 1.77$; C, $4/6(k=-1)$ in III MWT at $R^* = 2.50$; D, 4/6 in III WT at $R^* = 2.80$; E, 4/5 in III WT at $R^* = 4.42$; F, 4/0 in III T at $R^* = 7.22$; I, 2/0 in II T at $R^* = 1$; J, $2/6(S_P = 2-0)$ in III WTS_N at $R^* = 1.71$; K, $2/5(S_P = 1-0)$ in III WTS_N at $R^* = 2.80$; L, $2/0(S_P = 1-0)$ in III TS_N at $R^* = 5.05$; X, 2/0 in III T at $R^* = 7$; Y, 2/4 in III WT at $R^* = 6.46$; Z, $4/6(k=-1)$ in III MWT at $R^* = 2.62$. The transient N/m state and R^* value at each point are as follows: C′, 4/5 at $R^* = 2.50$; E′, 4/6 at $R^* = 4.42$; K′, $2/6(S_P = 2-0)$ at $R^* = 2.80$; L′, $2/5(S_P = 1-0)$ at $R^* = 5.05$; Z′, 2/4 at $R^* = 2.62$.

(E), where m changes with R^*, but N remains constant. Next, R^* is decreased from the 4/5 state at E, and the 4/5 state is maintained until $R^* = 2.50$ where the state transition from 4/5 (C′) to $4/6(k=-1)$ (C) occurs. Therefore, a hysteresis loop is completed between E and C. (If R^* is increased from the 4/5 state at E, the 4/5 state continues until $R^* = 7.22$ where the 4/0 state (F) is obtained.)

Figure 13(a–c) shows the wavenumber-increase mechanism for the travelling waves in the above transition, $N/m = 4/5$ (C′) $\rightarrow 4/6(k=-1)$ (C), where $\hat{t}$ is elapsed time and $t(=\hat{f}_0\hat{t})$ is its dimensionless time scaled by the rotation period of the inner sphere. First, one wave (labelled 5) of the five travelling azimuthal waves shown in figure 13(a) becomes flat and stretches in the azimuthal direction ϕ, as shown in figure 13(b). Next, the wave divides in half to become two waves (labelled 5 and 6), and consequently six azimuthal waves are completed, as shown in figure 13(c). The modulation ($k=-1$) of the six azimuthal waves fully develops after a few minutes. The wavenumber-decrease mechanism for the travelling waves in the state transition from 4/6 (E′) to 4/5 (E) at $R^* = 4.42$ is the reverse of the increase mechanism described above: two of the six waves first become flat, then become one wave.

The second example of hysteresis is obtained, as shown in figure 12, for the initial flow mode with a state of $N/m = 2/0$ at $R^* = 1$ (I). When R^* is first increased from 1 (I) to 7 (X), we obtain $m = 6$ between J and K′, $m = 5$ between K and L′ and $m = 0$ between L and X, keeping $N = 2$. Next, R^* is decreased from 7 (X) to just above 2.62 (Z′), and we obtain $m = 4$ between Y and Z′, still keeping $N = 2$. Hence, we observe the hysteresis by which different m values are obtained for cases with both increasing and decreasing R^*. This hysteresis is closely related to the fact that different

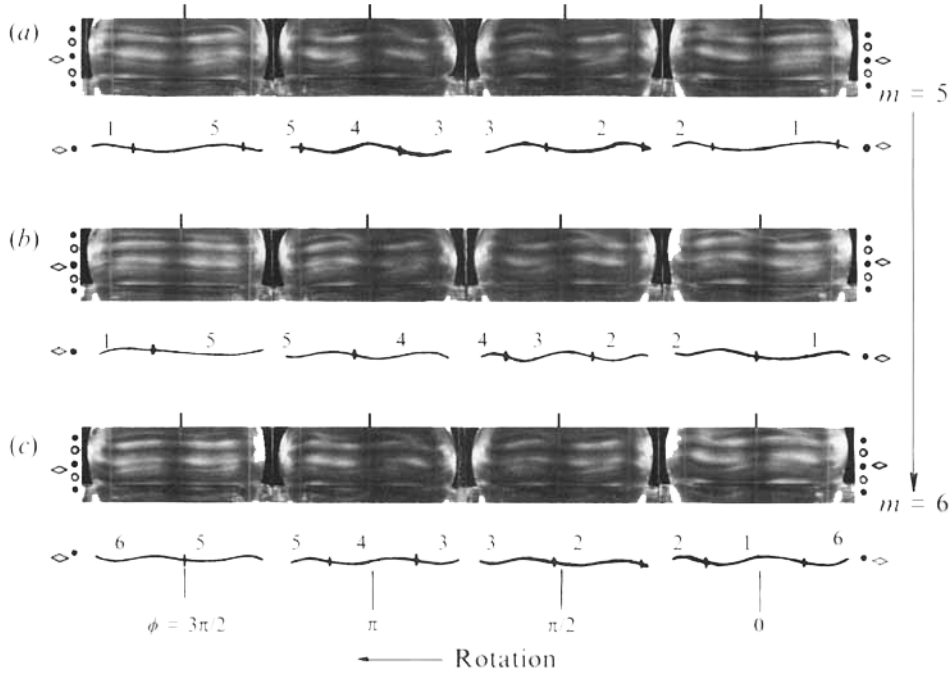

FIGURE 13. Wavenumber-increase mechanism for the travelling azimuthal waves in the state transition from $N/m = 4/5$ to $4/6(k = -1)$ at $R^* = 2.50$. The elapsed time $\hat{t}(t = f_0\hat{t})$ increases downward, and the azimuthal angle ϕ increases leftward. ϕ is measured in the laboratory and increases in the direction of sphere rotation. The vortex outflow and inflow boundaries are shown by ● and ○, respectively. The travelling waves on the outflow boundary at the equator are schematically drawn below each photograph. Successive waves around the annulus in the direction of the wave rotation are numerically indicated (1–m). The diamond indicates the position of the equator. (*a*) Five travelling azimuthal waves at $\hat{t} = 0$ s ($t = 0$). (*b*) Transient waves at $\hat{t} = 11$ s ($t = 4.1$). (*c*) Six travelling azimuthal waves at $\hat{t} = 24$ s ($t = 8.5$). (The modulation fully develops after a few minutes.)

numbers of spiral vortex pairs, S_P, are obtained in both cases, i.e. $S_P = 2-0$ (for $m = 6$, 5) or $S_P = 1-0$ ($m = 5$) in the case with increasing R^* but $S_P = 0-0$ ($m = 4$) for decreasing R^*.

When R^* is further decreased to just 2.62 (Z), then N increases from 2 to 4 (Z′ → Z), and consequently we obtain the travelling waves with $m = 6$ ($k = -1$) described previously. This increase of N shows that, without spiral vortices, the four-vortex flow in which the vortex outflow boundary is located at the equator is more stable than the two-vortex flow in which the vortex inflow boundary is located at the equator. Figure 14(*a–d*) shows the cell-number-increase mechanism for the toroidal vortices in the above transition from Z′ with $N/m = 2/4$ to Z with $4/6(k = -1)$. Figure 14(*a*) shows the initial state with $N = 2$. The cell-number increase is triggered by a new vortex which occurs on the inner-sphere wall in the central part of the upper cell of two toroidal vortex cells, as shown in the schematic of figure 14(*b*). Next, the newborn vortex grows toward the outer-sphere wall and simultaneously stretches in the azimuthal direction, as shown in figure 14(*c*). Finally, the newborn vortex develops into a toroidal vortex within the upper cell and consequently makes the upper cell divide into three toroidal vortex cells, shown in figure 14(*d*). Subsequently, six modulated azimuthal waves begin to develop on the vortex cells. The phenomenon described above shows a kind of dislocation.

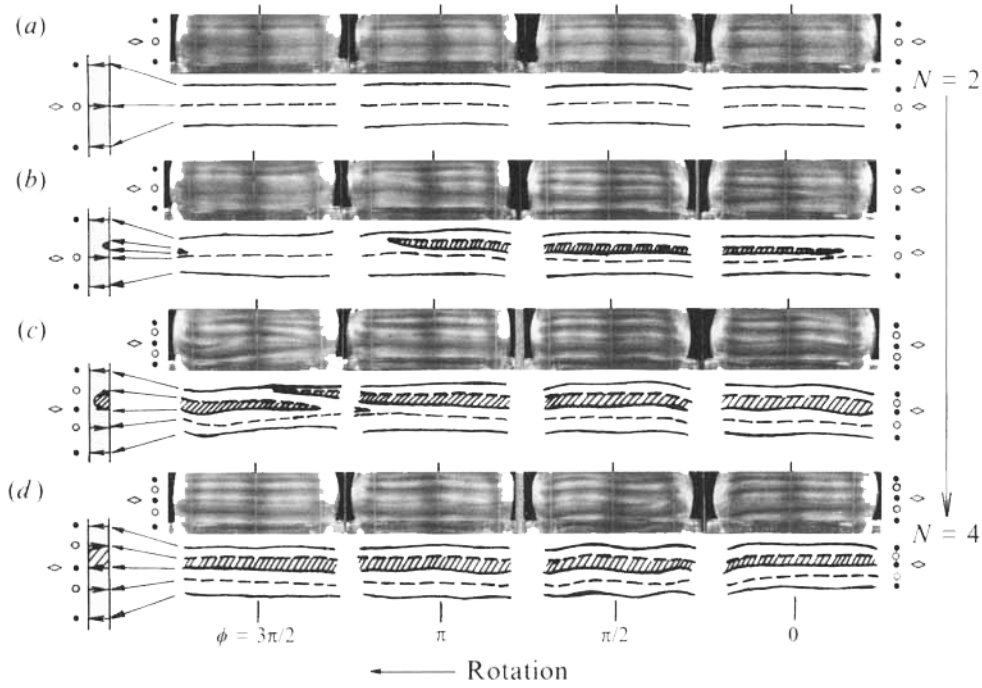

FIGURE 14. Cell-number-increase mechanism for the toroidal TG vortex cells in the state transition from $N/m = 2/4$ to $4/6 (k = -1)$ at $R^* = 2.62$. The elapsed time $\hat{t} (t = \hat{f}_0 \hat{t})$ increases downward, and the azimuthal angle ϕ increases leftward. The vortex outflow (●) and inflow (○) boundaries are schematically drawn by solid and dashed lines, respectively, below each photograph. The meridian cross-section of the TG vortices is also indicated schematically. The newborn vortex which occurs in the central part of the upper cell of two toroidal TG vortex cells is schematically indicated by hatching. The diamond indicates the position of the equator. (*a*) Two toroidal TG vortex cells at $\hat{t} = 0$ s ($t = 0$). (*b*) A newborn vortex is attached to the inner-sphere wall at $\hat{t} = 3.7$ s ($t = 1.5$). (*c*) The newborn vortex is developing toward the outer-sphere wall and in the streamwise (ϕ) direction at $\hat{t} = 16$ s ($t = 6.2$). (*d*) Four toroidal TG vortex cells at $\hat{t} = 18$ s ($t = 6.9$).

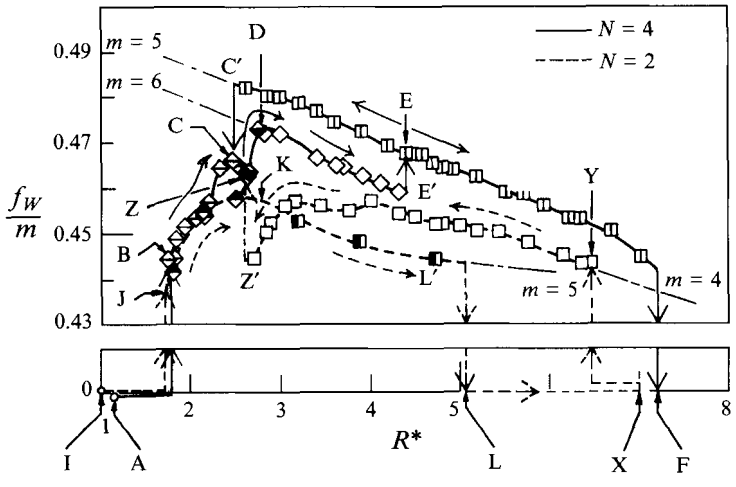

FIGURE 15. The hysteresis phenomenon appearing in the rotation frequency of travelling waves, corresponding to the hysteresis phenomenon shown in figure 12. Refer to figure 12 for labels A, B, C, ..., and to figure 10 for symbols ◆, ◧, ... The symbol □ shows the data for $m = 4 (N = 2)$ in III WT$(2.62 < R^* \leqslant 6.46)$.

Hysteresis appears not only in the above-described N/m state but also in the rotation frequency f_W/m of travelling waves shown in figure 15. The labels A, B, C, ... in figure 15 correspond to those in figure 12. A hysteresis loop appears between E and C for $N = 4$. This is because the rotation frequency of travelling waves depends on the wavenumber m. For the same reason, hysteresis also appears for $N = 2$.

6. Conclusions

In spherical Couette flow with the clearance ratio $\beta = 0.14$, we have considered how the characteristics of non-axisymmetric periodic disturbances in higher flow modes depend on the following three factors: (i) the rate of increase of the Reynolds number; (ii) the number of toroidal TG vortex cells in an initial flow mode; and (iii) the Reynolds-number history. Consequently, the following conclusions have been obtained.

The final flow mode at the Reynolds number R_S^* is independent of the rate of increase for $1 \leqslant R_S^* < 1.13$. For $R_S^* \geqslant 1.13$, however, the final flow mode does depend on the increase rate, so that a variety of final flow modes can be seen. This is because the final flow mode is determined by the relationship between the time taken to reach the R_S^* value and the viscous diffusion time required for development of TG vortices at that R_S^* value. In particular, provided that the time of increase is smaller than the viscous diffusion time for $R_S^* \gtrsim 3.3$ where the viscous diffusion time is more than 7.5 times the spin-up time, the supercritical basic flow III B is observed as the final flow mode.

The number N ($N = 4, 2, 0$) of toroidal vortex cells influences the rotation frequency and wavenumber for the cylinder-type disturbances as well as for the disk-type disturbances. Thus, the direction of secondary flow at the equator and the extension of the Ekman-type secondary flow have an important role in both the cylinder- and disk-type disturbances. This is linked with the sensitivity to the initial conditions in the transition to chaos.

Hysteresis due to different Reynolds-number histories appears even with a quasi-static increase or decrease of R^*. The phenomenon is manifested not only in the numbers N (toroidal vortex cells) and m (travelling waves) but also in the rotation frequency of the travelling waves. The latter hysteresis is due to the former, because the rotation frequency depends on the wavenumber.

REFERENCES

ANDERECK, C. D., DICKMAN, R. & SWINNEY, H. L. 1983 New flows in a circular Couette system with co-rotating cylinders. *Phys. Fluids* **26**, 1395.

BARTELS, F. 1982 Taylor vortices between two concentric rotating spheres. *J. Fluid Mech.* **119**, 1.

BONNET, J. P. & ALZIARY DE ROQUEFORT, T. 1976 Ecoulement entre deux sphères concentriques en rotation. *J. Méc.* **15**, 373.

BÜHLER, K. 1990 Symmetric and asymmetric Taylor vortex flow in spherical gaps. *Acta Mechanica* **81**, 3.

BÜHLER, K. & ZIEREP, J. 1987 Dynamical instabilities and transition to turbulence in spherical gap flows. In *Advances in Turbulence, Proc. 1st European Turbulence Conf.* (ed. G. Comte-Bellot & J. Mathieu), p. 16. Springer.

COLES, D. 1965 Transition in circular Couette flow. *J. Fluid Mech.* **21**, 385.

DENNIS, S. C. R. & QUARTAPELLE, L. 1984 Finite difference solution to the flow between two rotating spheres. *Computers Fluids* **12**, 77.

GORMAN, M. & SWINNEY, H. L. 1982 Spatial and temporal characteristics of modulated waves in the circular Couette system. *J. Fluid Mech.* **117**, 123.

KING, G. P., LI, Y., LEE, W., SWINNEY, H. L. & MARCUS, P. S. 1984 Wave speeds in wavy Taylor-vortex flow. *J. Fluid Mech.* **141**, 365.

MARCUS, P. S. 1984*a* Simulation of Taylor–Couette flow. Part 1. Numerical methods and comparison with experiment. *J. Fluid Mech.* **146**, 45.

MARCUS, P. S. 1984*b* Simulation of Taylor–Couette flow. Part 2. Numerical results for wavy-vortex flow with one travelling wave. *J. Fluid Mech.* **146**, 65.

MARCUS, P. S. & TUCKERMAN, L. S. 1987*a* Simulation of flow between concentric rotating spheres. Part 1. Steady states. *J. Fluid Mech.* **185**, 1.

MARCUS, P. S. & TUCKERMAN, L. S. 1987*b* Simulation of flow between concentric rotating spheres. Part 2. Transitions. *J. Fluid Mech.* **185**, 31.

NAKABAYASHI, K. 1983 Transition of Taylor–Görtler vortex flow in spherical Couette flow. *J. Fluid Mech.* **132**, 209.

NAKABAYASHI, K. & TSUCHIDA, Y. 1988*a* Spectral study of the laminar–turbulent transition in spherical Couette flow. *J. Fluid Mech.* **194**, 101.

NAKABAYASHI, K. & TSUCHIDA, Y. 1988*b* Modulated and unmodulated travelling azimuthal waves on the toroidal vortices in a spherical Couette system. *J. Fluid Mech.* **195**, 495.

NEWHOUSE, S., RUELLE, D. & TAKENS, F. 1978 Occurrence of Strange Axion A attractors near quasi-periodic flows on T^m, $m > 3$. *Commun. Math. Phys.* **64**, 35.

RAND, D. 1982 Dynamics and symmetry, predictions for modulated waves in rotating fluids. *Arch. Rat. Mech. Anal.* **79**, 1.

SAWATZKI, O. & ZIEREP, J. 1970 Das Stromfeld im Spalt zwischen zwei konzentrischen Kugelflächen, von denen die innere rotiert. *Acta Mechanica* **9**, 13.

WIMMER, M. 1976 Experiments on a viscous fluid flow between concentric rotating spheres. *J. Fluid Mech.* **78**, 317.

WIMMER, M. 1988 Viscous flows and instabilities near rotating bodies. *Prog. Aerospace Sci.* **25**, 43.

YAVORSKAYA, I. M., BELYAEV, YU. N., MONAKHOV, A. A., ASTAF'EVA, N. M., SCHERBAKOV, S. A. & VVEDENSKAYA, N. D. 1980 Stability, nonuniqueness and transition to turbulence in the flow between two rotating spheres. *Rep.* 595. Space Research Institute of the Academy of Science, USSR.